Review

Lithium insertion/extraction mechanism in alloy anodes for lithium-ion batteries

Wei-Jun Zhang

Department of Mechanical Engineering, Virginia Commonwealth University, 401 West Main Street, Richmond, VA 23284, United States

ARTICLE INFO

ABSTRACT

The electrochemical performance of alloy anodes has been reviewed in a previous paper [1]. In this work, the fundamental understanding of lithium-insertion/extraction mechanism in alloy anodes is discussed. The article summarizes the different types of lithium-reaction processes observed in Si, Sn, Sb, Al, Mg and their alloys, with particular emphasis on the characteristics unique to alloy anodes, including the sloping voltage profiles, lithiation amorphization, cycling hysteresis and reaction-potential depression. These unique characteristics are discussed with respect to the effect of interface and surface energies on the phase transformation and thermodynamic stability of fine alloy particles.

Contents

1. Introduction

Alloy anodes have been considered as one of the most promising electrode materials for next-generation lithium-ion batteries due to their high energy densities, relatively low cost, environmental compatibility and safe operation potentials. The disadvantages of alloy anodes include their short cycle life and high irreversible capacity loss as a result of the large volume expansion during lithium insertion [1–4]. In the last few years the electrochemical performance of alloy anodes has been significantly improved. For example, a long cycle life of 300 cycles at a capacity of 560 mAh g^{-1} has been reported for a SnSb nanocomposite [5]. In addition, high initial coulombic efficiencies of ~90% are obtained for a number of alloys [1]. The approaches used for achieving such improvement have been extensively reviewed in previous papers [1–4].

Besides the advances in electrochemical performance, great progress has been made in understanding the lithium-insertion/extraction processes in various alloy anodes from pure Si, Sn, Sb, Al and Mg to their alloy composites [6–68]. The basic

E-mail address: zweijun@vcu.edu.

reaction scheme and the corresponding structural change have been identified using in-situ XRD, high-resolution TEM and EELS analysis. However, there are still many questions that remain to be addressed. For example, it is not well understood why lithium insertion in Si anodes leads to amorphous products. It is also unclear why some anodes exhibit sloping voltage profiles instead of the flat voltage curves expected for a two-phase reaction.

In this report, the lithium-insertion/extraction processes in various alloy anodes are reviewed. The unique reaction characteristics of alloy anodes are discussed. The voltage profiles and peak reaction potentials of different alloy systems are compared. The analysis suggests that interface (or surface) energy appears to have a great impact on the lithium-reaction mechanism in alloy anodes.

2. Type of lithium reactions in alloy

The reaction of lithium with a metal or an alloy compound can be generally divided into two groups and three different types: group A: (1) *solid-solution (insertion)* reaction and (2) *addition* reaction; group B: (3) *displacement* reaction. Reactions (2) and (3) are also referred to as reconstitution reaction [6–8].

In group A reaction, lithium ions are added in the reactant phase without displacing (extruding) components from the reactant. The reaction can be described as:

$$Li + xM \Leftrightarrow LiM_x \qquad (1)$$

The reactant M can be an element or a compound. The reactions of lithium with pure elements fall into this category. Depending on whether or not a phase transformation takes place, these reactions can be further divided into two types as (1) *solid-solution* reaction and (2) *addition* reaction. In a solid-solution reaction, no phase or structure change occurs in the reactant M when Li enters into its framework structure (that is a topotactic reaction) [7]. In an addition reaction the phase structure of the lithiated LiM_x is different from the parent phase M; thus, the reaction involves phase change from M to LiM_x. Li insertion/extraction in crystalline Si, Sn, Al and Sb are considered as addition reactions because of the very limited solubility of lithium in these elements. The reactions of Li with Mg and amorphous Si are regarded as solid-solution reactions.

According to Gibbs phase rule, the number of degrees of freedom *f* in a closed system at equilibrium is given by $f = C - P$, where *C* is the number of independent components and *P* is the number of phases existing in the system under constant temperature and pressure [7]. For a solid-solution reaction in a Li–M binary system, where only one phase exists, $C = 2$ and $P = 1$; therefore, the electric potential of the reaction is a degree of freedom and varies with the lithium concentration, meaning that the voltage profile exhibits a sloping (round) shape. While for an addition reaction where two phases co-exist, the degree of freedom is zero for a binary system, thus the electrode potential under equilibrium conditions is independent of the overall composition. A constant plateau is expected on the voltage profile for the two-phase equilibrium region.

For group A reaction, the reaction potential E_A versus lithium under equilibrium conditions can be calculated from the Gibbs free-energy change of reaction (1) via Nernst Equation [7]:

$$E_A = -\frac{\Delta G_m}{nF} \qquad (2)$$

where ΔG_m is equivalent to the free energy of formation of product LiM_x, *n* is the number of electrons involved in the reaction, *F* is Faraday's constant.

In group B reaction or *displacement* reaction, lithium reacts with one component M of an alloy compound MN_y while the other component N is displaced or extruded from the parent phase [6,8]. The displaced element N can be inactive or active towards lithium. For the N-inactive compounds such as Cu_6Sn_5 [9], $CrSb_2$ [10], SnO [48] or Sn_2Fe [11], the reaction can be written generally as:

$$Li + xMN_y \rightarrow LiM_x + xyN \qquad (3)$$

Some displacement reactions are not reversible, and the extruded component N does not participate in the subsequent reaction cycles but acts as a buffering matrix. In this case, the displacement reaction (3) becomes an addition reaction (1) for element M.

The equilibrium potential of a displacement reaction for a ternary system Li–M–N is independent of the overall composition due to the presence of three phases in the reaction. Thus, a distinct potential plateau is expected on the voltage profile according to Gibbs phase rule. The reaction potential can be calculated using the Nernst equation (2). However, the Gibbs free-energy change for this reaction is the free energy of formation of product LiM_x subtracting the free energy required to cleavage x mole of compound MN_y. Consequently, the reaction equilibrium potential for compound MN_y is lower than that for pure element M.

When the displaced component N in reaction (3) is active, it reacts with lithium at a potential lower than that for element M. This reaction can be considered as a displacement reaction (3) plus an addition reaction for element N. The active/active alloy examples include SnSb [12], InSb [8] and Mg_2Si [13]. Many active/active displacement reactions are not completely reversible in later cycles and the two active components react with lithium independently as separate addition reactions.

3. Lithium insertion/extraction in various alloys

A number of elements are reactive to lithium; however, only five of them have been extensively studied, i.e., Si, Sn, Sb, Al and Mg, due to their low cost, abundant supply and environmental compatibility [1–3]. In this section, the reactions of lithium with these five elements and their alloys are reviewed.

3.1. Si-based anodes

Silicon has been widely investigated because of its high theoretical energy density (4200 mAh g^{-1}) [1,4]. Wen and Huggins [14] in an early study showed that the electrochemical reaction of lithium with silicon at 415 °C follows the equilibrium Li–Si phase diagram, and the reaction products are Li_2Si_7, Li_7Si_3, $Li_{13}Si_4$ and $Li_{22}Si_5$ with the onset potentials of 332, 288, 158, and 44 mV, respectively. The Li–Si reaction at room temperature does not appear to follow this scheme. In fact, Li insertion/extraction in silicon at room temperature has been reported to deviate far from the equilibrium prediction, and the cycling voltage curves are influenced by both the Si particle size and the depth of lithiation. Fig. 1 shows the typical voltage curves observed for Si anodes with the particle sizes of few microns [15–19]. The first-cycle alloying curves exhibit a single flat plateau at ~0.1 V, indicating a single two-phase addition reaction instead of the multi-phase reactions predicted by the equilibrium Li–Si phase diagram. Moreover, the subsequent alloying curves are round-shaped with no potential plateau at all. Meanwhile, the dealloying voltage curves show a strong dependence on the cut-off potential of alloying. If the anode is fully alloyed to 0 V, the dealloying curves exhibit a single plateau at ~0.4 V in all the cycles, followed by an upwardly sloping region (Fig. 1a). However, if the anode is alloyed to above 50 mV, the dealloying curves are round-shaped with no distinct plateau (Fig. 1b).
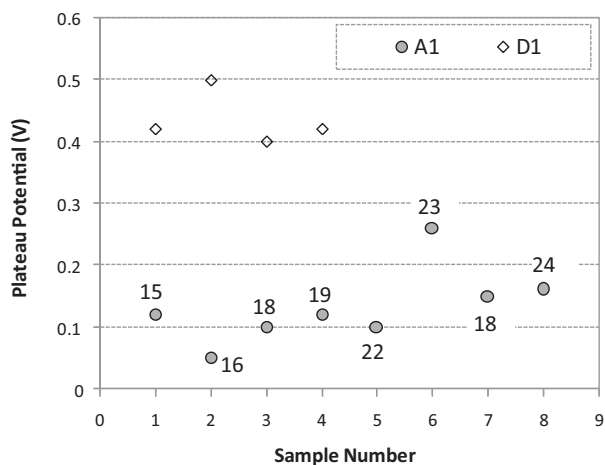
Detailed XRD studies [19–21] indicated that the crystalline Si particles are transformed to amorphous Li_xSi at above 50 mV in the first-alloying cycle. Because it is a two-phase addition reaction, a distinct plateau is observed. Below 50 mV, the amorphous phase is suddenly crystallized to $Li_{15}Si_4$ and the final lithiated product is
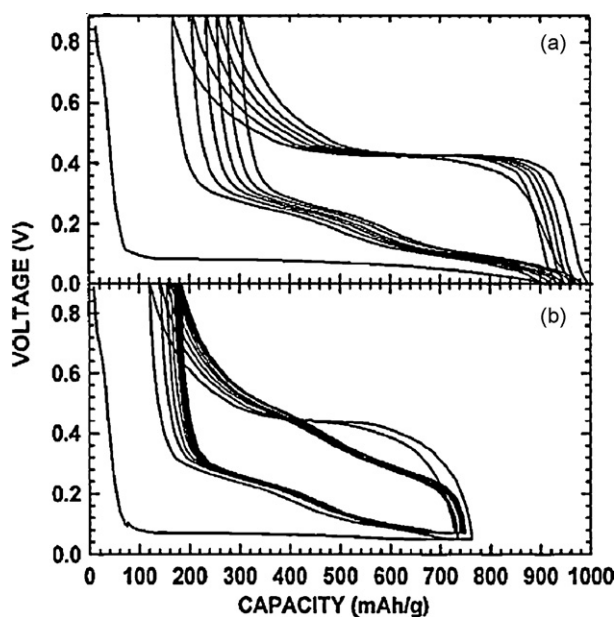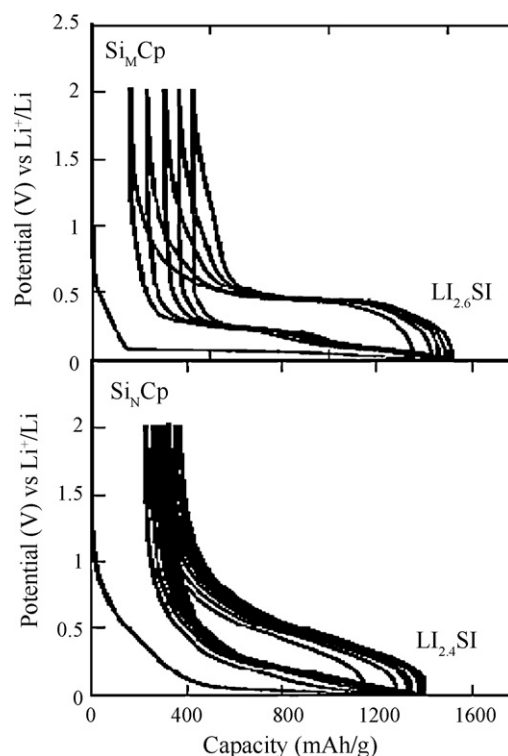
Fig. 1. Voltage curves of $Ni_{30}Si_{70}$ alloy (a) lithiated to 0 V and (b) lithiated to 50 mV for the first two cycles and then to 70 mV for later cycles [17]. Note that the voltage plateaus in dealloying cycles disappear when the cut-off voltage for alloying is 70 mV in (b). Reproduced with permission from The Electrochemical Society.

Fig. 3. Voltage–capacity curves for microsized (Si_M: 1–10 μm) and nanosized (Si_N: 10–100 nm) Si-anodes [18]. Reproduced with permission from Wiley-VCH.

crystalline $Li_{15}Si_4$. In this case, the subsequent dealloying curves exhibit a distinct plateau at ~0.4 V because of the two-phase reaction from crystalline $Li_{15}Si_4$ to amorphous Li_zSi ($z \approx 2$), followed by a solid-solution reaction from amorphous Li_zSi to amorphous Si [21]. When the anode is alloyed to above 0.5 mV with the amorphous Li_xSi as the final product, the subsequent delithiation process is a solid-solution reaction from amorphous Li_xSi to amorphous Si without phase change, leading to a sloping voltage curve. The voltages of alloying and dealloying plateaus reported for several Si-alloys at the first cycle are summarized in Fig. 2. The voltages of alloying plateaus are scattered around 0.1 V and the dealloying plateaus are at about 0.4 V.

The voltage profiles of Si anodes are also affected by the Si particle size. For Si particles of 50–200 nm, their dealloying curves are round-shaped with no distinct plateau, even after the anodes are fully alloyed to 0 V [18,25–30]. Fig. 3 shows an example where the micron-sized Si sample (S_MCp) has a flat dealloying plateau at

~0.4 V but the nanosized sample (S_NCp) (10–100 nm) shows a sloping dealloying curve even after fully alloyed to 0 V [18]. This type of behavior has been commonly observed in other studies [25–30]. When the Si particle sizes are further reduced to less than 20 nm, even the flat plateau at the first-alloying cycle turns to a sloping shape (i.e., all the voltage curves are round-shaped) [30–32].

For those sloping voltage curves, two broad peaks are often observed on the corresponding differential-capacity (dQ/dV) plots in both the alloying and dealloying regimes (see Fig. 4). The peak potentials of most Si-alloys distribute at ~0.06 V (A_a) and ~0.25 V (A_b) for alloying, and ~0.3 V (D_a) and ~0.5 V (D_b) for dealloying as shown in Fig. 5. The structural changes responsible for these peaks are not clearly understood yet. It may be a result of short-range ordering in the amorphous Li_xSi-alloys. An in-situ Mossbauer spectroscopy study of amorphous Si–Li alloys suggested that the nearest neighbors for each Si atom change from Si atoms to Li atoms at the composition of $Li_{2.3}Si$ during alloying [34].
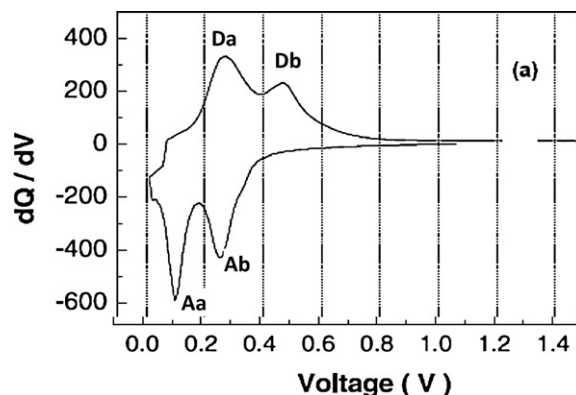

Fig. 2. The plateau voltages of the first-alloying cycle (A1) and the dealloying cycle (D1) observed in several microsized Si-anodes. Reference numbers are given in the graph.

Fig. 4. The differential capacity vs. potential curves for the 2nd charge-discharge cycle of a pure Si thin-film anode [33].
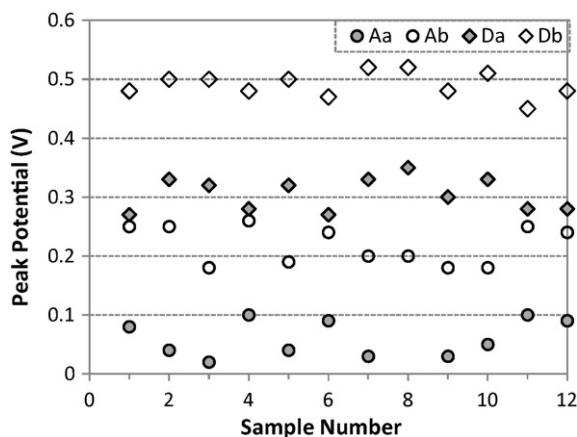
Fig. 5. The peak potentials reported in the differential capacity vs. voltage curves for silicon-alloy anodes in alloying (A_a and A_b) and dealloying (D_a and D_b) cycles [18,19,23–33].

Similarly, the voltage curves and phase transformation in amorphous Si thin-film anodes are affected by the film thickness, surface roughness and alloy additions [20,30,31]. It has been reported that the crystalline $Li_{15}Si_4$ phase forms only in amorphous Si films with a thickness larger than the critical value of ~2 μm (similar to the critical particle size for Si powders) [20]. Thicker Si films exhibit flat dealloying-voltage curves, while thinner films show sloping curves. However, Kim et al. [30] observed in a multilayer amorphous Fe/Si anode that crystallization becomes evident when the Si layer is thicker than 200 nm. They further noted that the formation of crystalline $Li_{15}Si_4$ phase is suppressed when the film is deposited on a rough surface. The relatively low critical thickness for crystallization in the Fe/Si films as compared to pure Si films may arise from the promoting effect of Fe/Si interfaces on the crystallite nucleation.

The displacement reaction of lithium with Si-based alloys such as $CaSi_2$ [35], $FeSi_6$ [24], TiSi [36] and Mg_2Si [13] has been investigated. The voltage profiles of these Si-based anodes are similar to those of pure Si anodes as mentioned above. Lithium insertion in Mg_2Si was claimed to form a ternary intercalated compound Li_xMg_2Si [13].

3.2. Sb-based anodes

In contrast to Si-alloys, the voltage profiles of most Sb anodes exhibit well-defined plateaus during alloying and dealloying [37–41]. Fig. 6a shows an example of an Sb/C nanocomposite with the Sb particle size of 10–30 nm. It appears that the voltage profiles of Sb anodes are not affected by their particle size if the particles are larger than 10 nm. However, when the particle sizes are smaller than 5 nm, the voltage curves become round-shaped as shown in Fig. 6b for a Ti_2Sb-alloy. The Ti_2Sb particles were converted into fine Sb crystals of 2–3 nm through displacement reaction after the first cycle [40]. It appears that the critical particle size for the transition from flat to sloping voltage curves for Sb-alloys is about 5 nm, which is smaller than that for Si-alloys (~20 nm).

Fig. 7 summarizes the plateau voltages for the first-cycle alloying (A1), the later-cycle alloying (A2) and the first-cycle dealloying (D1) for Sb and Sb-based alloys. The alloying and dealloying voltages for pure Sb anodes are ~0.85 V and ~1.05 V, respectively. The plateau voltages for the later cycles are quite close to those of the first cycle. However, the first-cycle alloying potentials for some Sb-based alloys are obviously lower than that of pure Sb anodes, e.g., 0.33 V for $TiSb_2$, 0.65 V for Cu_2Sb and 0.4 V for $NbSb_2$. After the first-alloying cycle, the reaction voltages of Sb-based alloys are
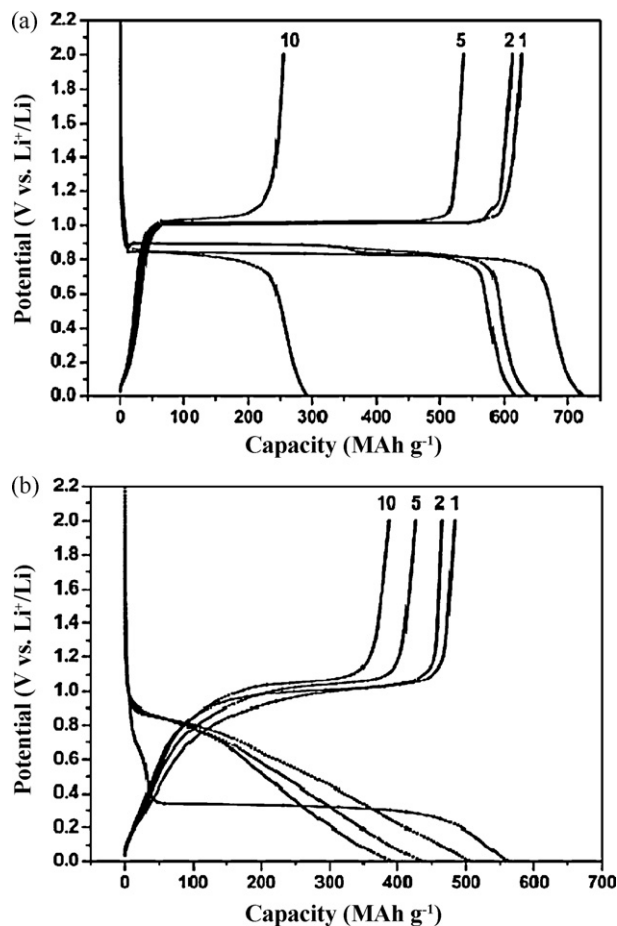
Fig. 6. Voltage profiles of (a) an Sb electrode and (b) a $TiSb_2$ electrode after the 1st, 2nd, 5th and 10th cycles [40]. Reproduced with permission from The Electrochemical Society.

very close to those of pure Sb anodes. The lower alloying potentials for Sb-based alloys at the first cycle is due to the reduced free-energy change (ΔG) in Eq. (2), because additional energy is required to extrude component M from the M_xSn-alloy in a displacement reaction.

Fig. 7. The plateau voltages of Sb-based alloy anodes: A1 (first-cycle alloying), A2 (later-cycle alloying), D1(first or later-cycle dealloying). The references are given in the graph.

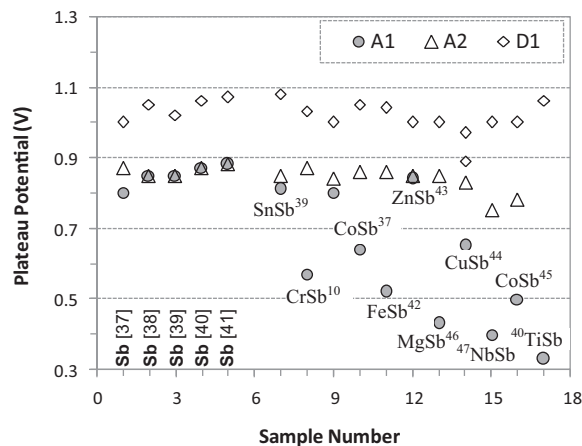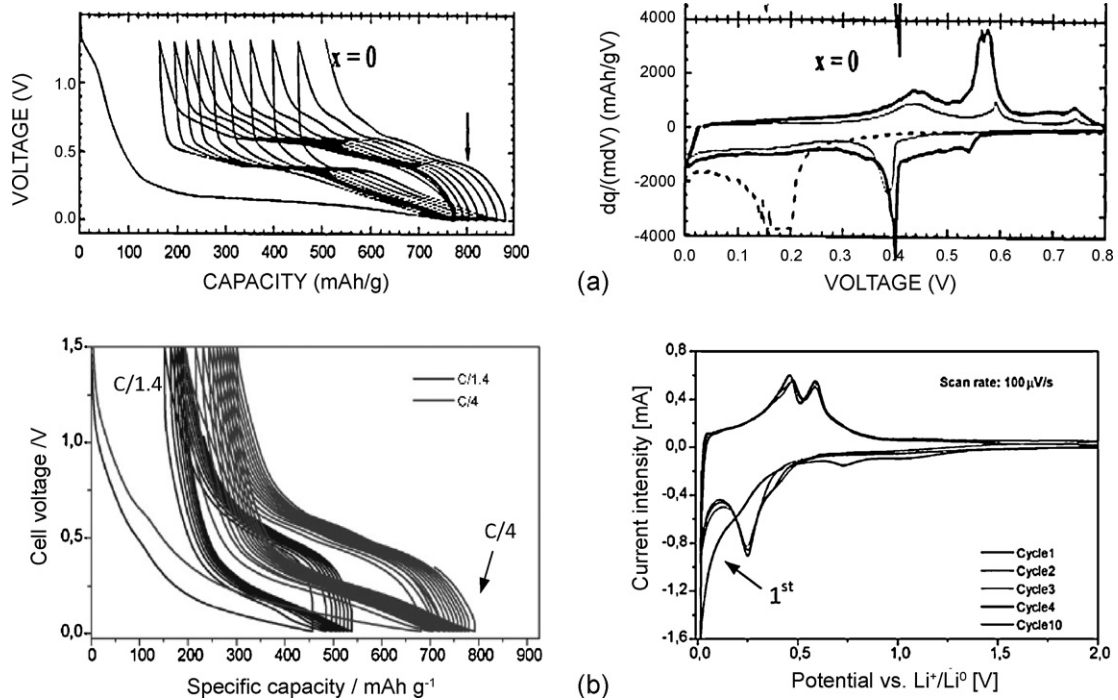**Fig. 8.** Voltage profiles and the corresponding differential-potential peaks for (a) Sn_2Fe [11] and (b) CoSn-alloy anodes [51].

3.3. Sn-based alloys

The Li–Sn binary-phase diagram suggests that there are eight crystalline phases at room temperature: Sn, Li_2Sn_5, LiSn, Li_7Sn_3, Li_5Sn_2, $Li_{13}Sn_5$, Li_7Sn_2 and $Li_{22}Sn_5$. The lithium-reaction potentials for Li_ySn phases determined from the coulombic titration curves at room temperature are: 0.66 ($y = 0.4–0.7$, $Sn–Li_2Sn_5$), 0.53 ($y = 0.7–2.33$, $LiSn–Li_7Sn_3$), 0.485 ($y = 2.33–2.6$, $Li_5Sn_2–Li_{13}Sn_5$), 0.42 ($y = 2.6–3.5$, $Li_{13}Sn_5 \sim Li_7Sn_2$) and 0.38 V ($y = 3.5–4.4$, $Li_7Sn_2–Li_{22}Sn_5$) (49). Some of the predicted equilibrium reactions have been confirmed by the in-situ XRD analysis of a Li–SnO cell. The dominant phases during the lithium-alloying regime were identified to be Sn (0.66 V), Li_2Sn_5 (0.55 V) and LiSn (0.41 V) (48, 50). The formation of Li-rich phases such as Li_7Sn_3 and $Li_{22}Sn_5$ at below 0.31 V was observed but could not be distinguished exclusively, because the structures of these phases are quite similar. The final lithiated product in Sn-based alloys was determined to be $Li_{22}Sn_5$. During delithiation the XRD patterns indicated the formation of LiSn at 0.78 V and Sn at 1.0 V. The dealloying potentials are apparently higher than the equilibrium values.

Although some equilibrium-lithiation products have been observed in Li–Sn cells, the voltage curves of many Sn-based anodes do not have a distinct plateau as expected for a two-phase reaction. Fig. 8 shows the voltage profiles and the corresponding differential-capacity curves for two Sn-based alloys. The first alloy (Sn_2Fe) has round-shaped curves with one or two less-defined plateaus [11], while the second alloy (CoSn) has completely sloped voltage profiles [51]. For both alloys, broad peaks are observed on the differential-capacity curves.

The differential-capacity peaks reported for Sn and Sn-based alloys are compared in Fig. 9. For pure Sn anodes there are normally three peaks observed in the alloying regime and four peaks in the dealloying (a differential-capacity curve for pure Sn is shown in Fig. 10). For the Sn-based alloys only one or two peaks are observed. This result suggests that the lithium-reaction mechanism in Sn-based alloys strongly depends on the alloy composition. The peak potentials are quite consistent for all the alloys shown in Fig. 9:

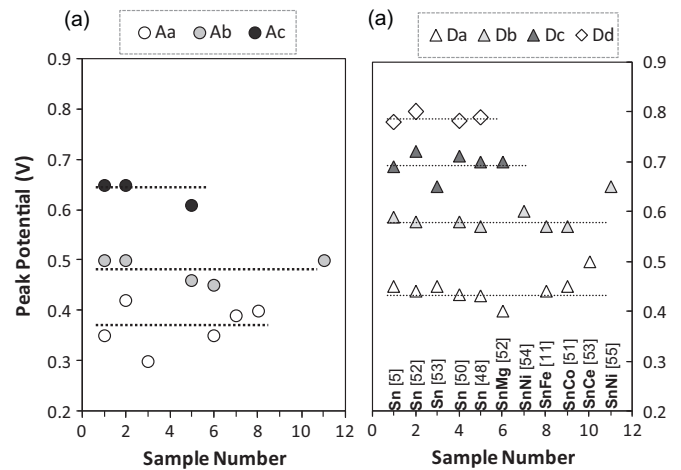**Fig. 9.** Peak potentials on the differential capacity vs. voltage curves for (a) alloying and (b) dealloying cycles of Sn-alloy anodes. Pure Sn anodes (samples 1–5) normally exhibit three peaks in alloying (Aa, Ab and Ac) and four peaks in dealloying (Da, Db, Dc and Dd). Reference and alloy type are given in the graph.
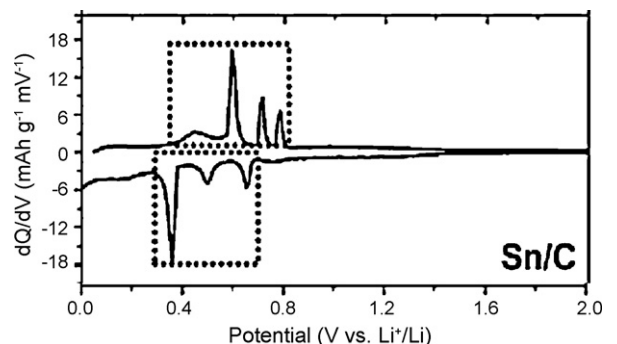

Fig. 10. The differential capacity vs. voltage curves for a Li–Sn cell [5].

0.36, 0.48 and 0.65 V in alloying, and 0.42, 0.56, 0.69 and 0.78 V in dealloying. Based on the in-situ XRD result aforesaid [48], it is reasonable to speculate that the first two peaks in the alloying cycle (0.65 V and 0.48 V) and the last two peaks in dealloying cycle (0.69 V and 0.78 V) correspond to the Sn–Li_2Sn_5 and Li_2Sn_5–LiSn reactions, respectively. The lack of distinct plateaus on the voltage curves of Sn-based alloys will be further discussed in later section.

3.4. Intermetallic alloys

Lithium reaction with intermetallic alloys such as Cu_6Sn_5, SnSb, InSb and Cu_2Sb has been extensively investigated [8,9,12,44,56]. The purpose of using compound alloys is to create a Li-insertion host that maintains a strong structural relationship with the intermediate and the lithiated phases to minimize the volume expansion during reaction [44,57]. Generally, the reactions of lithium with intermetallic alloys are displacement reactions because one component is extruded from the parent compound during lithiation. However, it has been reported that lithium insertion in several intermetallic alloys results in the formation of intercalated products such as Li_xInSb [38,58,59], Li_2CuSn [60] and Li_2CuSb [9,61,62]. For example, Thackeray and co-workers [60,61] proposed based on in-situ XRD analysis that the lithiation of Cu_2Sb took place by forming an intermediate phase, $Li_{2-x}Cu_{1+x}Sb$ ($x = 0–1$), with the concurrent extrusion of amorphous Cu before the formation of final lithiated product Li_3Sb.

3.5. Al and Mg alloys

In the Al–Li system there are three possible lithiated products LiAl, Li_3Al_2 and Li_9Al_4 at room temperature according to the binary phase diagram [63]. However, it was observed in electrochemical tests that lithium insertion in aluminum led to the formation of LiAl with a maximum capacity of 992 mAh g^{-1}, although crystalline LiAl was not identified by the XRD analysis [63–65]. The reaction exhibits a single voltage plateau at ~0.26 V in alloying and ~0.43 V in dealloying during the first cycle [63,65].

The Li–Mg binary alloy system is a very attractive anode candidate, because a solid-solution Li–Mg region covers the entire range from 30% to nearly 100 at.% Li [3,66]. Only a few studies have been performed on the Li–Mg alloys due to the low reaction potential and high reactivity of Mg [13,66,67]. The lithium insertion in Mg occurs at a potential very close to that of Li-metal, which raises safety concerns related to lithium deposition [13,52,67,68]. Two phases were identified by the XRD analysis during the Li insertion in Mg: one Mg-rich phase (α) and one Li-rich phase (β). Two corresponding peaks were observed in the differential-capacity curves [67]. The Li-extraction from Mg-rich phase was observed to be only partially reversible, which may limit the cyclic performance of Mg-containing alloys [67,68].

4. Discussion

The reaction of lithium with alloy anodes is a complicated process, which involves the conventional nucleation and growth of new phases along with charge transfer, volume expansion, plastic deformation and grain refinement [6]. As discussed above, the lithium-insertion/extraction processes in alloy anodes exhibit several unique features such as (a) amorphization in silicon, (b) sloping voltage profiles for small particles and (c) cycling-voltage hysteresis. In this section, these unique characteristics are discussed in relation to the influence of several factors on the thermodynamics and kinetics of phase transformation in alloy particles. One factor of particular interest is the effect of interface energy on the nucleation and growth of a new phase in alloy system. Interface energy has been reported to significantly affect the phase
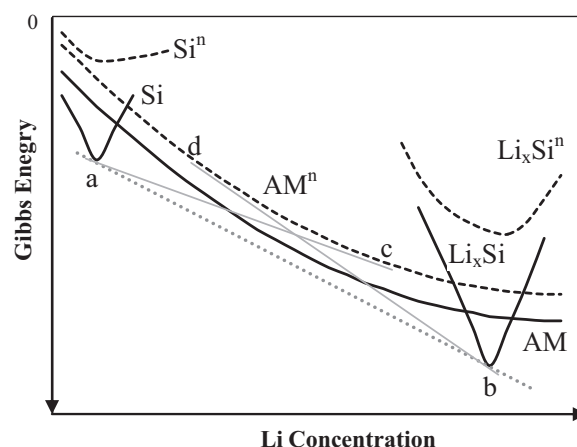

Fig. 11. Schematic illustration of the equilibrium Gibbs free-energy curves for crystalline Si, lithiated phase Li_xSi and amorphous phase AM at infinite sizes (solid lines); and the total free-energy curves for the corresponding nuclei of small sizes: Si^n, Li_xSi^n and AM^n (dash lines). The total free energy of a stable nucleus is higher (less negative) than the equilibrium Gibbs free energy due to the additional interface energy.

transformation in nano-scaled materials [69–75]. For example, the high-temperature fcc-γ phase can be stabilized at room temperature in Fe crystals if the crystal size is smaller than 50 nm [71]. Modeling and experimental studies also suggested that high interface and surface energies may alter the voltage profiles of nanosized lithium-insertion materials such as TiO_2 and $FePO_4$ [71–77]. Note that the current discussion is not intended to provide solid answers to the challenge questions but to intrigue more studies in this area.

4.1. Silicon amorphization

As mentioned in section 3.1, lithium insertion in crystalline Si and its alloys leads to the formation of amorphous products rather than the equilibrium crystalline phases (Li_xSi). Amorphization also takes place in the dealloying cycles. It was proposed in a previous paper that the amorphization of silicon was due to the lower free energy (less negative) of the metastable amorphous Li–Si phase compared to the equilibrium crystalline phases [78]. The lower voltage plateau of 0.1 V observed in the first-alloying cycle as compared to the equilibrium potential of 0.33 V was considered in the previous study as a proof of the low free energy of the amorphous phase. According to their proposed model, the cycling voltages of Si anodes in the following alloying cycles should be in the range of 0–0.1 V due to the much lower free energy of the amorphous Li_xSi phase. In contrast, many Si anodes cycled in the voltage range of 0–0.3 V in the subsequent alloying cycles (from amorphous Si to amorphous Li_xSi), which are very close to the equilibrium voltages for crystalline phases (see Fig. 1). These experimental results indicate that the free energy of amorphous Li_xSi phase seems to be quite close to that of the crystalline Li_xSi alloy.

The formation of amorphous Li–Si phase instead of crystalline Li_xSi alloy in Si anodes is probably due to the large nucleation-energy barrier for the formation of crystalline Li_xSi phase, resulting from the high interface energy (and strain energy) [70,71,78]. To facilitate the discussion, a schematic illustration of the energy curves for the Li–Si system is shown in Fig. 11. The free energy of the amorphous Li–Si phase (AM, solid line) under the equilibrium condition is higher than that of the two-phase mixture of Si and Li_xSi (the dotted line a–b). Therefore, a two-phase region of Si + Li_xSi is predicted in the equilibrium phase diagram. Note that the equilibrium free-energy curves (the solid lines) of Si, Li_xSi and AM phases refer to the phases of infinite size. In other words, the
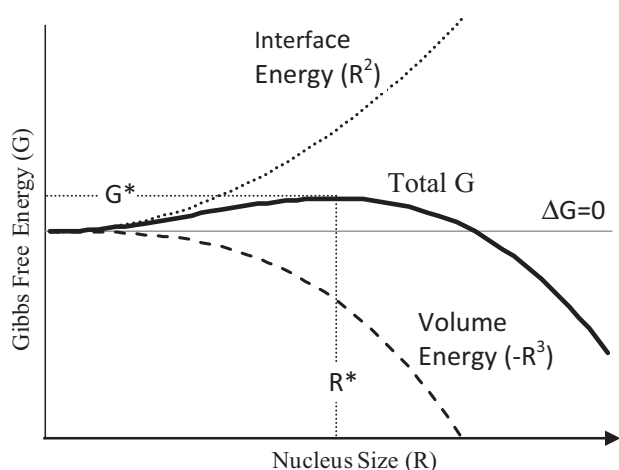
Fig. 12. The total free energy of a spherical nucleus as a function of the nucleus size. A stable nucleus must overcome the maximum nucleation-energy barrier G^* and attain the critical nucleus size R^* to grow continuously.

grain (or particle) sizes of the said phases are large enough that the interface (or surface) energy is negligible compared to the volume energy of the phase.

But in a real alloy system, the formation of a new phase β in a parent phase α starts with a nucleus of very small size and the growth of this nucleus needs to overcome an energy barrier G^*, as illustrated in Fig. 12, because the formation of nucleus β in α phase creates an interface between them. The interface energy (positive) increases with r^2 while the volume energy (negative) decreases with r^3, where r is the radius for a spherical nucleus. As a result, the total free energy (G) of the system is actually positive at the early stage of nucleation, see Fig. 12, and the nucleus is thermodynamically unstable until it reaches the critical size R^* at the maximum energy G^*. A higher interface energy leads to a larger critical nucleus size R^*.

Because of their close-packed lattice structure, metal and alloy phases are expected to have much higher interface (surface) energies than those compounds with low packing densities. Phase transformation in metals and alloys may thus be more dramatically affected by the interface energy. As illustrated in Fig. 11, the actual total energy of a stable Li_xSi nucleus (Li_xSi^n, dash line) formed in a parent Si phase is well above the equilibrium free energy of that phase (Li_xSi, solid line). Similarly, the total formation energy of a stable amorphous Li–Si nucleus (AM^n, dash line) is also expected to be higher than the equilibrium value (AM, solid line). It is plausible to assume that the interface energy and the resultant energy increase for amorphous phase are lower than that for the crystalline phase because of the disordered structure and low packing density of amorphous phase. Therefore, the formation of a stable amorphous Li–Si nucleus (AM^n) is thermodynamically more favorable than the formation of a crystalline nucleus Li_xSi^n due to the higher total energy of the latter (Fig. 11). As a result, lithium insertion in Si takes place as a two-phase reaction from crystalline Si to amorphous Li–Si (gray solid line a–c) instead of the equilibrium reaction from Si to crystalline Li_xSi (dotted line a–b). The relatively low reaction potential for the formation of amorphous nucleus (AM^n) (i.e., the slope of line a–c) as compared to the equilibrium potential for crystalline Li_xSi (the slope of line a–b) may originate from the lower free energy of amorphous phase and the higher interface energy for the crystalline nucleus.

The same scenario may occur during the lithium-extraction reaction if the lithiated phase is crystalline Li_xSi (i.e., $Li_{15}Si_4$ phase). Instead of forming crystalline Li–Si or Si phase according to the equilibrium line b–a, an amorphous Li–Si nucleus grows follow-

ing the line b–d in Fig. 11. If no crystalline phase formed in the first-alloying regime, lithium extraction from the amorphous Li_xSi phase is thus a solid-solution reaction with no phase change (following the AM free-energy curve if the particle is large enough). The same process repeats in the later cycles when the lithium insertion/extraction takes place in the amorphous phases, resulting in sloping voltage curves as observed in Fig. 1. Obviously, this hypothesis needs to be validated by further modeling and experimental works.

4.2. Formation of crystalline $Li_{15}Si_4$ phase

The sudden crystallization of $Li_{15}Si_4$ phase in coarse Si powders/films after lithiated to below 50 mV can also be interpreted based on the hypothesis discussed above. As shown in Fig. 11, lithium insertion in amorphous Li_xSi phase increases the Li concentration toward the end composition of $Li_{15}Si_4$ [21]. The total energy of the lithiated phase is between the line AM^n and line AM depending on the size of the amorphous particle. At the end of lithiation, the composition of amorphous phase Li_xSi is very close to that of the crystalline phase ($Li_{15}Si_4$). The equilibrium free energy of the crystalline phase (point b) is lower (more negative) than that of the amorphous phase. But phase transformation from amorphous Li_xSi to crystalline $Li_{15}Si_4$ through nucleation is still not feasible because of the required high interface energy. However, phase change without nucleation is thermodynamically favorable if the particle size of the amorphous phase is large enough that the increase of surface/interface energy due to crystallization is minimal compared to the decrease of volume energy. Phase transformation can proceed via a non-diffusional process with no composition change (e.g., martensitic transformation). In this case, once the phase transformation takes place, the entire amorphous particle will transform suddenly into crystalline phase through the short-range atom rearrangement [70]. A similar process has been proposed for lithium insertion in nanosized TiO_2 and $FePO_4$ materials [73,79].

Note that the sudden crystallization occurs only in relatively large Si particles. For smaller particles, crystallization is thermodynamically unfavorable because the required interface energy increase from amorphous to crystalline $Li_{15}Si_4$ particles cannot be compensated by the volume-energy decrease due to the large surface areas of small particles. This may explain why crystallization has been observed only in microsized Si powders and films (>2 μm) [19,20]. An exceptional situation is when the crystallized $Li_{15}Si_4$ phase can develop a coherent interface with the surrounding matrix so that the interface-energy increase is minimized. The observation of crystalline $Li_{15}Si_4$ formation in a thinner (~200 nm) Fe/Si multilayer film appears to be such a case [30]. The formation of a coherent interface between the crystalline $Li_{15}Si_4$ and Fe layers is expected to reduce the total interface energy, therefore, crystallization can take place in a relatively thinner film. This speculation consists with the observation that crystallization was suppressed when the film was deposited on a rough surface where a coherent interface (straight) could not be established. The observation of crystalline $Li_{15}Si_4$ solely in large microsized Si particles indicates that the interface/surface energies of crystalline Li_xSi-alloys are considerably high.

4.3. Voltage curve hysteresis

The voltage curves of alloy anodes often display a gap between the alloying and dealloying cycles, and the plateau voltages in alloying cycles are always lower than those in dealloying cycles (see Figs. 1, 6 and 8). This cycling hysteresis has been considered in several papers as a result of polarization due to kinetic limitations. However, it was found in a detailed study that the gap could not be eliminated by reducing the current rates or by taking into account

of the heat released. Instead, the gap was likely resulted from the activation energy required for bond-breaking [80]. As shown in Figs. 5, 7 and 9, the plateau or peak voltages reported in different studies are quite consistent for each alloy system (Si, Sb and Sn). These systematic shifts were not likely resulted from electrode polarization but from the additional energy required for nucleation as shown in Fig. 11.

Taking the Sb-alloy as an example (Fig. 7), the alloying and dealloying plateau voltages for Sb and Sb-based alloys are ~0.85 V and ~1.05 V, respectively (except for the first-alloying cycle for some Sn-based alloys). The equilibrium-reaction potentials for the formation of Li_2Sb and Li_3Sb are 0.948 V and 0.956 V, respectively [49]. This means that the voltage plateaus of Sb anodes shift lower in alloying cycles and higher in dealloying cycles by about 0.1 V versus the equilibrium potential of ~0.95 V. A similar behavior was also observed in Si-alloys (Fig. 5); the dealloying peak voltages of 0.3 V and 0.5 V are ~0.25 V higher than the corresponding alloying peak voltages of 0.06 V and 0.25 V, although the exact phase transformation responsible for these peaks is not completely clear. This systematic shift of reaction voltages may be related to the interface-energy (and strain energy) terms added in the Nernst equation (2). For insertion materials with low interface energy and small volume change, the reaction potential can be calculated from the Gibbs formation energy (ΔG_m) using the Eq. (2). But for alloy anodes with high interface energy and large volume change, the interface and strain energies required for creating a lithiated phase at a stable size is not insignificant. Therefore, an additional-energy term ΔG_{is} (interface + strain energy) needs to be added in the Nernst equation (2). The term ΔG_{is} is always positive, whereas the ΔG_m is negative for alloying and positive for dealloying. Therefore, the addition of ΔG_{is} results in a lower potential in alloying cycles and a higher potential in dealloying cycles relative to the equilibrium potential, as being widely observed in Si and Sb-based alloys. A similar potential shift is also expected to be seen in Sn-based anodes (Fig. 9) if the complex reaction scheme for these alloys is clarified.

4.4. Sloping voltage curves for nanosized alloy anodes

The voltage profiles of alloy anodes tend to become sloped when their particle sizes are small. Nanosized Si-alloys (Fig. 3) and Sn-alloys (Fig. 8b) exhibit entirely sloped voltage curves in both the alloying and dealloying cycles, even though flat voltage curves are expected for all these anodes according to the Gibbs phase rule. The voltage profiles of Sb-alloys also become round-shaped when their particle sizes are smaller than 5 nm (Fig. 6b).

Voltage curve rounding-off has been observed in other nanosized insertion materials [75,76,81]. The sloping voltage curves observed in nanosized TiO_2 and $FePO_4$ have been attributed to the increased solid-solution region between the pristine and lithiated phases, resulting from the high surface or interface energies in nanosized particles [71,73,77]. As shown in Fig. 12, as the particle size decreases, the total energy of a two-phase reaction in a small particle will be dominated by the surface/interface energy instead of volume energy. As a result, the energy gain due to phase separation (that is forming a second-phase nucleus), represented by the free energy of mixing, will decrease for small particles. The nucleation of a new phase in these particles will eventually become thermodynamically unstable when their particle sizes are smaller than a critical value, and the particles prefer to form a solid solution with Li over the whole compositional range [73]. In other words, the thermodynamically-favorable reaction changes from addition reaction for large particles to solid-solution reaction for smaller particles. The sloping voltage curves observed in nanosized alloy particles may thus be considered as a result of extended solid solution with Li in these alloy particles. Modeling of the surface-energy effect in nanosized particles suggests that reducing the particle size

to a certain extent leads to the rounding-off of the voltage curves and the shift of reaction potential [71,72,74]. According to one model, a broad particle size distribution in nanosized alloy powders may also lead to a varied reaction potential [74].

The sloping voltage profiles of nanosized alloy powders can also be interpreted from the structural point of view. Nanosized materials can be considered to consist of two components: a crystalline component formed by all atoms located in the crystal lattice and an interfacial component of the atoms located at the interface (surface). The interface (surface) component can be considered as amorphous material because their atoms are randomly located [82]. For a material with its crystal size smaller than 10 nm, the volume fraction of the interfacial/surface component is higher than 50%. Therefore, these tiny particles can be treated partially as amorphous particles, in which Li insertion/extraction takes place through a solid-solution reaction.

The critical particle size for the transition from a flat to sloping voltage curve is ~20 nm for Si-anodes and ~5 nm for Sb anodes. The larger critical size for Si-alloys compared to Sb-alloys is another indication that the surface, and interface energies of Si-alloys are relatively high.

4.5. Potential impacts on battery-cell design

Understanding the lithium-reaction mechanisms has significant implications on battery design and performance prediction. In particular, the dependence of voltage profiles on particle sizes in alloy anodes needs to be seriously considered. It is well known that alloy particles subject to particle refinement (to few nanometers) during repeated cycling [5,40,83]. Accordingly, the performance such as energy output of the battery cells with an alloy electrode may be progressively altered in their service life due to the change of particle size. Furthermore, the tiny alloy particles formed during cycling refinement are energetically unstable due to their high surface energy. They tend to merge or agglomerate into large particles or form surface-electrolyte-interface films especially at relatively high operation temperature. This may in turn change the voltage profiles of the cells. Therefore, it is vitally important to examine the long-term cyclic and calendar performance of alloy electrodes. The influence of charge rate on the lithium-reaction mechanism in alloy anodes also needs further consideration.

It has been reported that the migration of trace amount of transition metal ions from cathodes such as $LiFePO_4$ or $LiMn_2O_4$ to the graphite anode severely degrade the cyclic performance of lithium-ion batteries due to their catalytic effect on the formation of SEI films [84,85]. The influence of metal ion contamination on the performance of alloy anodes is not expected to be as severe as in graphite anodes because a trace amount of these transition metals are likely soluble in alloy anodes.

5. Conclusions

The lithium-insertion/extraction mechanisms in Si, Sb, Sn, Al, Mg and their alloys are reviewed. Lithium reactions in alloy anodes can be generally divided into (a) solid-solution reaction, (b) addition reaction and (c) displacement reaction. The reaction mechanism appears to depend strongly on the alloy particle size. The voltage curves of smaller alloy particles tend to be round-shaped. The formation of crystalline $Li_{15}Si_4$ was observed only in microsized powders after lithiated to below 50 mV. Lithium reaction with silicon at room temperature does not follow the equilibrium scheme and amorphous lithiated products are generally observed instead of crystalline compounds. The formation of amorphous products in Si-alloys and the dependence of voltage profiles on alloy particle sizes are likely related to the high interface (surface) energies of alloy particles.

The voltage curves of alloy anodes exhibit a distinct alloying/dealloying hysteresis. The alloying voltage plateaus are normally lower than the dealloying potentials. This voltage hysteresis appears to arise from the additional interface energies required for the nucleation and growth of reaction products.

Acknowledgements

References

[1] W.J. Zhang, J. Power Sources 196 (2011) 13.
[2] M. Winter, J.O. Besenhard, M.E. Spahr, P. Novak, Adv. Mater. 10 (1998) 725.
[3] D. Larcher, S. Beattie, M. Morcrette, K. Edstrom, J.C. Jumas, J.M. Tarascon, J. Mater. Chem. 17 (2007) 3759.
[4] U. Kasavajjula, C. Wang, A.J. Appleby, J. Power Sources 163 (2007) 1003.
[5] C.M. Park, H.J. Sohn, Electrochim. Acta 54 (2009) 6367.
[6] R. Benedek, M.M. Thackeray, J. Power Sources 110 (2002) 406.
[7] A. Anani, R.A. Huggins, J. Power Sources 38 (1992) 351.
[8] M. Wachtler, M. Winter, J.O. Besenhard, J. Power Sources 105 (2002) 151.
[9] S. Matsuno, M. Noji, M. Nakayama, M. Wakihara, Y. Kobayashi, H. Miyashirob, J. Electrochem. Soc. 155 (2008) A151.
[10] F.J. Fernandez-Madrigal, P. Lavela, C. Perez-Vicente, J.L. Tirado, J. Electroanaly. Chem. 501 (2001) 205.
[11] O. Mao, R.A. Dunlap, J.R. Dahn, J. Electrochem. Soc. 146 (1999) 405.
[12] J. Yang, Y. Takeda, N. Imanishi, J.Y. Xie, O. Yamamoto, Solid State Ionics 133 (2000) 189.
[13] H. Kim, J. Choi, H.J. Sohn, T. Kang, J. Electrochem. Soc. 146 (1999) 4401.
[14] C.J. Wen, R.A. Huggins, J. Solid State Chem. 37 (1981) 271.
[15] J.H. Ryu, J.W. Kim, Y.E. Sung, S.M. Oh, Electrochem. Solid-State Lett. 7 (2004) A306.
[16] Q. Si, K. Hanai, N. Imanishi, M. Kubo, A. Hirano, Y. Takeda, O. Yamamoto, J. Power Sources 189 (2009) 761.
[17] Z. Luo, D. Fan, X. Liu, H. Mao, C. Yao, Z. Deng, J. Power Sources 189 (2009) 16.
[18] J. Saint, M. Morcrette, D. Larcher, L. Laffont, S. Beattie, J.P. Peres, D. Talaga, M. Couzi, J.M. Tarascon, Adv. Funct. Mater. 17 (2007) 1765.
[19] M.N. Obrovac, L. Christensen, Electrochem. Solid-State Lett. 7 (2004) A93.
[20] T.D. Hatchard, J.R. Dahn, J. Electrochem. Soc. 151 (2004) A838.
[21] J. Li, J.R. Dahn, J. Electrochem. Soc. 154 (2007) A156.
[22] C.S. Wang, G.T. Wu, X.B. Zhang, Z.F. Qi, W.Z. Li, J. Electrochem. Soc. 145 (1998) 2751.
[23] J.P. Maranchi, A.F. Hepp, P.N. Kumta, Electrochem. Solid-State Lett. 6 (2003) A198.
[24] T. Li, Y.L. Cao, X.P. Ai, H.X. Yang, J. Power Sources 184 (2008) 473.
[25] G.X. Wang, J. Yao, H.K. Liu, Electrochem. Solid-State Lett. 7 (2004) A250.
[26] G.X. Wang, J.H. Ahn, J. Yao, S. Bewlay, H.K. Liu, Electrochem. Commun. 6 (2004) 689.
[27] S. Ohara, J. Suzuki, K. Sekine, T. Takamura, J. Power Sources 119–121 (2003) 591.
[28] P.K. Chan, H. Peng, G. Liu, K. Mcilwrath, X.F. Zhang, R.A. Huggins, Y. Cui, Nat. Nanotechnol. 3 (2008) 31.
[29] L.B. Chen, J.Y. Xie, H.C. Yu, T.H. Wang, J. Appl. Electrochem. 39 (2009) 1157.
[30] J.B. Kim, S.H. Lim, S.M. Lee, J. Electrochem. Soc. 153 (2006) A455.
[31] H.Y. Lee, S.M. Lee, Electrochem. Commun. 6 (2004) 465.
[32] J. Graetz, C.C. Ahn, R. Yazami, B. Fultz, Electrochem. Solid-State Lett. 6 (2003) A194.
[33] J.B. Kim, H.Y. Lee, K.S. Lee, S.H. Lim, S.M. Lee, Electrochem. Commun. 5 (2003) 544.
[34] J. Li, A. Smith, R.J. Sanderson, T.D. Hatchard, R.A. Dunlap, J.R. Dahn, J. Electrochem. Soc. 156 (2009) A283.
[35] J. Wolfenstine, J. Power Sources 124 (2003) 241.
[36] K.M. Lee, Y.S. Lee, Y.W. Kim, Y.K. Sun, S.M. Lee, J. Alloys Compd. 472 (2009) 461.
[37] R. Alcantara, F.J. Fernandez-Madrigal, P. Lavela, J.L. Tirado, J.C. Jumas, J. Olivier-Fourcade, J. Mater. Chem. 9 (1999) 2517.
[38] K.C. Hewitt, L.Y. Beaulieu, J.R. Dahn, J. Electrochem. Soc. 148 (2001) A402.
[39] H. Li, L. Shi, W. Lu, X. Huang, L. Chen, J. Electrochem. Soc. 148 (2001) A915.
[40] C.M. Park, H.J. Sohn, J. Electrochem. Soc. 157 (2010) A46.
[41] C.M. Park, S. Yoon, S.I. Lee, J.H. Kim, J.H. Jung, H.J. Sohn, J. Electrochem. Soc. 154 (2007) A917.
[42] C. Villevieille, B. Fraisse, M. Womes, J.C. Jumas, L. Monoconduit, J. Power Sources 189 (2009) 324.
[43] B. Zhao, G.S. Cao, Electrochim. Acta 46 (2001) 891.
[44] M. Morcrette, D. Larcher, J.M. Tarascon, K. Edstrom, J.T. Vaughey, M.M. Thackeray, Electrochim. Acta 52 (2007) 5339.
[45] J.M. Tarascon, M. Morcrette, L. Dupont, Y. Chabre, C. Payen, D. Larcher, V. Pralong, J. Electrochem. Soc. 150 (2003) A732.
[46] H. Honda, H. Sakaguchi, I. Tanaka, T. Esaka, J. Power Sources 123 (2003) 216.
[47] M.A. Reddy, U.V. Varadaraju, J. Power Sources 159 (2006) 336.
[48] I.A. Courtney, J.R. Dahn, J. Electrochem. Soc. 144 (1997) 2045.
[49] J. Wang, I.D. Raistrick, R.A. Huggins, J. Electrochem. Soc. 133 (1986) 457.
[50] P.P. Ferguson, R.A. Dunlap, J.R. Dahn, J. Electrochem. Soc. 157 (2010) A326.
[51] J. Hassoun, S. Panero, G. Mulas, B. Scrosati, J. Power Sources 171 (2007) 928.
[52] H. Kim, Y.J. Kim, D.G. Kim, H.J. Sohn, T. Kang, Solid State Ionics 144 (2001) 41.
[53] H. Sakaguchi, H. Honda, Y. Akasaka, T. Esaka, J. Power Sources 119–121 (2003) 50.
[54] J. Hassoun, S. Panero, B. Scrosati, J. Power Sources 160 (2006) 1336.
[55] H. Qin, X. Zhao, N. Jiang, Z. Li, J. Power Sources 171 (2007) 948.
[56] T. Sarakonsri, C.S. Johnson, S.A. Hackney, M.M. Thackeray, J. Power Sources 153 (2006) 319.
[57] L. Fransson, E. Nordstrom, K. Edstrom, L. Haggstrom, J.T. Vaughey, M.M. Thackeray, J. Electrochem. Soc. 149 (2002) A736.
[58] C.S. Johnson, J.T. Vaughey, M.M. Thackeray, T. Sarakonsri, S.A. Hackney, L. Fransson, K. Edstrom, J.O. Thomas, Electrochem. Commun. 2 (2000) 595.
[59] J.T. Vaughey, J. O'Hara, M.M. Thackeray, Electrochem. Solid-State Lett. 3 (2000) 13.
[60] K.D. Kepler, J.T. Vaughey, M.M. Thackeray, J. Power Sources 81–82 (1999) 383.
[61] L.M.L. Fransson, J.T. Vaughey, R. Benedek, K. Edstrom, J.O. Thomas, M.M. Thackeray, Electrochem. Commun. 3 (2001) 317.
[62] C. Villevieille, C.M. Ionic-Bousquet, B. Ducorant, J.C. Jumas, L. Monoconduit, J. Power Sources 172 (2007) 388.
[63] Y. Hamon, T. Brousse, F. Jousse, P. Topart, P. Buvat, D.M. Schleich, J. Power Sources 97–98 (2001) 185.
[64] M.J. Lindsay, G.X. Wang, H.K. Liu, J. Power Sources 119–121 (2003) 84.
[65] D. Larcher, L.Y. Beaulieu, O. Mao, A.E. George, J.R. Dahn, J. Electrochem. Soc. 147 (2000) 1703.
[66] T.J. Richardson, G. Chen, J. Power Sources 174 (2007) 810.
[67] C. Park, Y.U. Kim, H. Kim, H.J. Sohn, J. Power Sources 158 (2006) 1451.
[68] D. Larcher, A.S. Prakash, J. Saint, M. Morcrette, J.M. Tarascon, Chem. Mater. 16 (2004) 5502.
[69] Q. Meng, N. Zhou, Y. Rong, S. Chen, T.Y. Hsu, Acta Mater. 50 (2002) 4563.
[70] Q. Meng, Y. Rong, T.Y. Hsu, Phys. Rev. B 65 (2002) 174118.
[71] M. Wagemaker, F.M. Mulder, A. Van der Ven, Adv. Mater. 21 (2009) 2703.
[72] A. Van der Ven, M. Wagemaker, Electrochem. Commun. 11 (2009) 881.
[73] M. Wagemaker, W.J.H. Borghols, F.M. Mulder, J. Am. Chem. Soc. 129 (2007) 4323.
[74] M.N. Obovac, J.R. Dahn, Phys. Rev. B 61 (2000) 6713.
[75] G. Sudant, E. Baudrin, D. Larcher, J.M. Tarascon, J. Mater. Chem. 15 (2005) 1263.
[76] N. Meethong, H.Y.S. Huang, W.C. Carter, Y.M. Chiang, Electrochem. Solid State Lett. 10 (2007) A134.
[77] G. Kobayashi, S. Nishimura, M.S. Park, R. Kanno, M. Yashima, T. Ida, A. Yamada, Adv. Funct. Mater. 19 (2009) 395.
[78] P. Limthongkul, Y.I. Jang, N.J. Dudney, Y.M. Chiang, J. Power Sources 119–121 (2003) 604–609.
[79] C. Delmas, M. Maccario, L. Croguennec, F. Le Cras, F. Weill, Nat. Mater. 7 (2008) 665.
[80] V.L. Chevrier, J.R. Dahn, J. Electrochem. Soc. 157 (2010) A392.
[81] A. Yamada, H. Koizumi, S.I. Nishimura, N. Sonoyama, R.J. Kanno, M. Yonemura, T. Nakamura, Y. Kobayashi, Nat. Mater. 5 (2006) 357.
[82] X. Zhu, R. Birringer, U. Herr, H. Gleiter, Phys. Rev. B 35 (1987) 9085.
[83] I. Rom, M. Wachtler, I. Papst, M. Schmied, J.O. Besenhard, F. Hofer, M. Winter, Solid State Ionics 143 (2001) 329.
[84] H.F. Jin, Z. Liu, Y.M. Teng, J.K. Gao, Y. Zhao, J. Power Sources 189 (2009) 445.
[85] K. Amine, J. Liu, I. Belharouak, Electrochem. Commun. 7 (2005) 669.